Progress In Electromagnetics Research C, Vol. 170, 15–27, 2026

PIER C

(Received 7 March 2026, Accepted 10 April 2026, Scheduled 4 May 2026)

A Deadbeat Fault-Tolerant Control Strategy for PMSM Demagnetization Faults Based on an Improved Flux Linkage Observer

Yang Zhang*, Wancheng Xie, Yang Gao, Jiahao Zhang, and Moutao Li

Hunan University of Technology, Zhuzhou 412007, China

ABSTRACT: To address issues such as reduced motor output performance and diminished load capacity caused by permanent magnet demagnetization in Permanent Magnet Synchronous Motor (PMSM), a super-twisting algorithm-based fault-tolerant predictive control strategy for demagnetization faults in PMSM is proposed. First, the improved super-twisting non-singular fast terminal sliding mode observer (IST-NFTSMO) is constructed to accurately observe the flux linkage and predict the current at the next moment. Based on the observed values, a deadbeat fault-tolerant predictive control (DFTPC) algorithm is built to compensate for the torque loss due to permanent magnet demagnetization, thereby achieving fault-tolerant control of the system. Second, a sliding mode controller based on a novel reaching law is designed, thereby overcoming the shortcomings of traditional control strategies in PMSM vector control systems, such as poor anti-interference capability and slow response speed. Finally, experimental results demonstrate that after a demagnetization fault occurs in the PMSM, the proposed method effectively improves the fault tolerance capability of the PMSM system while ensuring the dynamic response speed of the control system, thereby endowing the system with enhanced stability and robustness.

1. INTRODUCTION

In recent years, PMSM has been widely employed in numerous industrial fields, such as robotics, vehicles, and wind power generation due to its advantages of simple structure and fast dynamic response [1–4]. Owing to its unique permanent magnet structure, demagnetization may occur under the influence of various natural and human factors, including high temperature, impact, and corrosion. This can lead to irreversible demagnetization faults in the PMSM, resulting in phenomena such as decreased electromagnetic torque, reduced output capability, and a significant increase in stator current [5, 6]. Therefore, both the diagnosis of demagnetization faults in PMSMs and the implementation of fault-tolerant control post-failure hold significant theoretical research value and practical engineering importance.

Currently, three main methods are distinguished for addressing demagnetization faults in PMSM: methods based on signal analysis, methods based on data processing, and methods based on mathematical models [7].

The fault diagnosis method based on signal analysis achieves fault diagnosis by measuring signals such as motor voltage, current, and magnetic flux, followed by processing and analyzing these signals to extract fault characteristics [8]. To detect demagnetization faults in PMSM, in [9], demagnetization is inferred by online acquisition of various electrical signals from the faulty motor, and by comparing the differences in harmonic content between a healthy motor and a partially demagnetized motor. Under demagnetization fault conditions, ref. [10] analyzes different demagnetization scenarios using the calculated power spectral density features of the stator current, obtained through finite element analysis. Ref. [11] aims to achieve demagnetization fault detection by measuring various performance indicators of noise during PMSM operation, such as acoustic fluctuations and sound roughness. Ref. [12] extracts demagnetization fault information of the PMSM using noise and vibration signals, enabling online diagnosis of motor demagnetization faults.

Fault diagnosis methods based on data processing typically involve training artificial intelligence for fault diagnosis using extensive operational data from faulty conditions, enabling diagnosis under complex scenarios in engineering applications. In [13], demagnetization faults of permanent magnets are diagnosed by analyzing the response characteristics of faulty motors under high-frequency signal injection. However, this operation can only be performed while the motor is stopped, making real-time fault detection unfeasible. Ref. [14] utilizes a deep learning convolutional neural network architecture to diagnose PMSM demagnetization faults, but it is only applicable for fault diagnosis at constant motor speeds and requires a substantial volume of data. Ref. [15] introduces a method that combined image morphological texture feature extraction with a cuckoo search-optimized spiking neural network algorithm. This method addresses the fine quantitative diagnosis and identification of demagnetization faults in dual-primary permanent magnet synchronous linear motors.

Fault diagnosis methods based on mathematical models achieve fault diagnosis by constructing a mathematical model

---

* Corresponding author: Yang Zhang (459387623@qq.com).

doi:10.2528/PIERC25030706

Published by THE ELECTROMAGNETIC ACADEMY

of the motor to estimate its states or parameters, and by monitoring the discrepancies between the motor's actual performance and its predicted performance. Ref. [16] proposes a method based on an adaptive state observer. The designed observer can simultaneously and accurately identify the motor d-q axis inductances and flux linkages, enabling the detection of demagnetization faults in PMSM under conditions of parameter variation. Ref. [17] presents a method based on a cascaded adaptive sliding mode observer. The adaptive observer and the sliding mode observer are arranged in a cascaded structure, allowing them to compensate for each other. This enables the detection of demagnetization faults in PMSM even under time-varying stator resistance. Ref. [18] uses multiple observers combined with estimation errors to calculate the flux linkage for detecting demagnetization faults in PMSM. This eliminates the influence of inductance mismatch. However, its accuracy depends on the precision of the observer's output. Ref. [19] designs an adaptive linear neuron model reference flux linkage observer. This solves the problem of accurate online flux linkage observation for permanent magnet synchronous linear motors under multiple operating conditions. By comparing with precise flux linkage values, it diagnoses faults and their severity.

To enable stable and normal motor operation despite demagnetization faults, ref. [20] proposes a fault-tolerant control method based on equivalent input disturbance. By incorporating a decoupling term into the observer, the influence of motor speed on demagnetization fault reconstruction is eliminated. This method, combined with the equivalent input disturbance approach, achieves fault-tolerant control for demagnetization faults. Ref. [21] introduces the concept of active flux linkage and reestablishes the PMSM mathematical model that includes active flux linkage. A deadbeat control strategy is adopted to eliminate active flux linkage errors, thereby achieving the objective of fault-tolerant control. Ref. [22] utilizes an adaptive observer to accurately estimate flux linkage, thereby obtaining observed values of the state currents. These values are then fed back to the controller, achieving fault-tolerant control with online detection. Ref. [23] proposes a parameter identification method based on a high-frequency signal equivalent impedance model for PMSM. An algorithm incorporating parameter sensitivity analysis is introduced. By injecting high-frequency signals, the flux linkage is identified, which is utilized for detecting the coupling between resistance and flux linkage. Ref. [24] designs an axial flux compensation to mitigate demagnetization faults in PMSM; however, its use of a look-up table method results in low accuracy and limited effectiveness. Ref. [25] proposes a robust fault-tolerant predictive current control algorithm based on a composite observer, which can eliminate the effects of motor parameter disturbances and permanent magnet demagnetization.

In summary, a deadbeat fault-tolerant control strategy based on an improved super-twisting non-singular fast terminal sliding mode observer is proposed in this paper. For demagnetization faults in PMSM, this strategy enables faster and more accurate fault detection, achieves torque compensation under demagnetization conditions, and ensures stable motor operation even after a demagnetization fault occurs. The main contributions of this work are as follows:

(1) The improved super-twisting control law is combined with the nonsingular fast terminal sliding mode surface. As a result, the IST-NFTSMO with faster convergence speed is designed. With this observer, the d-axis and q-axis flux linkage components of the PMSM before and after permanent magnet demagnetization can be estimated more rapidly and accurately.

(2) To achieve superior fault-tolerant performance, the DFTPC algorithm is introduced. Following permanent magnet demagnetization, this algorithm promptly outputs the reference current for the d-axis at the next time step. This compensates for the torque deficit, suppresses the sudden surge of the q-axis current, and enables the q-axis current and electromagnetic torque to quickly return to their values under normal motor operation.

(3) To further enhance system stability and response speed, an improved exponential reaching law is combined with an integral sliding mode surface to form the improved sliding mode controller (ISMC). When integrated with a sliding mode disturbance observer (SMDO), the controller exhibits enhanced anti-interference capability, thereby achieving better fault-tolerant performance.

2. PMSM MATHEMATICAL MODEL

2.1. The Conventional Mathematical Model of PMSM

Neglecting losses, such as eddy current loss and hysteresis loss, the mathematical model of the PMSM in the d-q coordinate system can be expressed as [26]:

$$\left\{\begin{array}{l} u_d = R_s i_d + \frac{d\psi_d}{dt} - \omega_e \psi_q \\ u_q = R_s i_q + \frac{d\psi_q}{dt} + \omega_e \psi_d \end{array}\right. \tag{1}$$

where R_s is the stator resistance; ω_e is the electrical angular velocity; u_d, u_q, i_d, i_q, ψ_d, ψ_q are the d-q axis stator voltages, stator currents, stator flux linkages, respectively.

The electromagnetic torque equation of the PMSM in the d-q coordinate system is expressed as:

$$T_e = \frac{3}{2} n_p \left[\psi_{ro} + (L_d - L_q)\, i_d\right] i_q \tag{2}$$

where T_e is the electromagnetic torque; L_d and L_q are the d-axis and q-axis stator inductances, respectively; n_p is the number of pole pairs; ψ_{ro} is the permanent magnet flux linkage.

The flux linkage equations are:

$$\left\{\begin{array}{l} \psi_d = \psi_{ro} + L_d i_d \\ \psi_q = L_q i_q \end{array}\right. \tag{3}$$

The mechanical motion equation of PMSM can be expressed as:

$$\frac{d\omega_e}{dt} = \frac{n_p}{J} \left(T_e - T_L - B\omega_m\right) \tag{4}$$

where ω_m is the mechanical angular velocity; J is the rotational inertia; T_L is the load torque; B is the viscous friction coefficient.

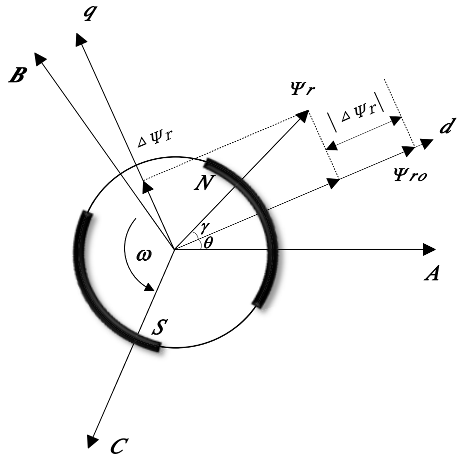

FIGURE 1. Variation relationship of PM flux linkage.

2.2. The Demagnetization Mathematical Model of PMSM

Under the influence of various factors, such as high temperature and corrosion, demagnetization of the permanent magnets may be induced in a PMSM. The magnitude of its flux linkage will change from the initial value ψ_{r0} to ψ_r, and a deviation angle γ will be generated between the field orientation direction and the flux linkage direction [27] (see Figure 1). The flux linkage equations are rewritten as:

$$\begin{cases} \psi_d = \psi_{r_0} + \Delta\psi_{rd} + L_d i_d = \psi_{rd} + L_d i_d \\ \psi_q = \Delta\psi_{rq} + L_q i_q = \psi_{rq} + L_q i_q \end{cases} \tag{5}$$

where $\Delta\psi_{rd}$ and $\Delta\psi_{rq}$ are variables of the PM flux on the d-q axis, $\Delta\psi_{rd} = \psi_r \cos\gamma - \psi_{r0} < 0$, $\Delta\psi_{rq} = \psi_r \sin\gamma > 0$; ψ_{rd} and ψ_{rq} are two new components of ψ_r on the d-q axis, $\psi_{rd} = \psi_r \cos\gamma$, $\psi_{rq} = \psi_r \sin\gamma$.

The mathematical model for a PMSM under a demagnetization fault is given as:

$$\begin{cases} u_d = R_s i_d + L_d \frac{di_d}{dt} - \omega_e \psi_{rq} - \omega_e L_q i_q \\ u_q = R_s i_q + L_q \frac{di_q}{dt} + \omega_e L_d i_d + \omega_e \psi_{rd} \end{cases} \tag{6}$$

The electromagnetic torque equation for a PMSM under a demagnetization fault is expressed as:

$$T_e = \frac{3}{2} n_p \left[\psi_{rd} i_q + (L_d - L_q) i_d i_q - \psi_{rq} i_d\right] \tag{7}$$

3. DESIGN OF THE DFTPC

When a PMSM experiences a demagnetization fault under the $i_d = 0$ control mode, maintaining a constant electromagnetic torque inevitably leads to a sharp increase in i_q. However, the output capability of the inverter is limited. The i_q during demagnetization approaches its maximum allowable value, making it impossible to compensate for the lost electromagnetic torque by further adjusting i_q. Consequently, fault-tolerant control can only be achieved by regulating i_d. Deadbeat control, in theory, enables the actual value of the controlled variable to perfectly match its reference value within one or several control cycles, allowing for precise control of the motor torque. Based on this concept, the effective flux linkage after the fault can be made to track an appropriate value within a control cycle, thereby compensating for the lost electromagnetic torque through the adjustment of i_d.

Under normal operating conditions, the effective flux linkage of the PMSM is given by:

$$\psi_{ext} = \psi_{ro} + (L_d - L_q) i_d \tag{8}$$

Under demagnetization fault conditions, the effective flux linkage of the PMSM is given by:

$$\psi_{ext-f} = \psi_{rd} + (L_d - L_q) i_d \tag{9}$$

The flux linkage equations for a PMSM under demagnetization fault conditions are given as:

$$\begin{cases} \psi_d = \psi_{ext-f} + L_q i_d \\ \psi_q = \psi_{rq} + L_q i_q \end{cases} \tag{10}$$

Performing first-order Eulerian discretization on (10) yields:

$$\begin{cases} \psi_d(k) = \psi_{ext-f}(k) + L_q i_d(k) \\ \psi_q(k) = \psi_{rq}(k) + L_q i_q(k) \end{cases} \tag{11}$$

From (11), the flux linkage equation at time $k+1$ can be acquired:

$$\begin{cases} \psi_d(k+1) = \psi_{ext-f}(k+1) + L_q i_d^{ref}(k+1) \\ \psi_q(k+1) = \psi_{rq}(k+1) + L_q i_q(k+1) \end{cases} \tag{12}$$

where $i_d^{ref}(k+1)$ is the d-axis reference current at the next time.

Substituting (10) into (1) yields:

$$\begin{cases} \dot{\psi}_d = -\frac{R_s}{L_q}\psi_d + \omega_e \psi_q + u_d + \frac{R_s}{L_q}\psi_{ext-f} \\ \dot{\psi}_q = -\frac{R_s}{L_q}\psi_q - \omega_e \psi_d + u_q + \frac{R_s}{L_q}\psi_{rq} \end{cases} \tag{13}$$

Performing first-order Eulerian discretization on (13), the state equation of the PMSM under a demagnetization fault is obtained as:

$$\begin{cases} \psi_d(k+1) = \left(1 - T_s \frac{R_s}{L_q}\right)\psi_d(k) + T_s \omega_e(k) \psi_q(k) \\ \qquad + T_s u_d(k) + T_s \frac{R_s}{L_q}\psi_{ext-f}(k) \\ \psi_q(k+1) = -T_s \omega_e(k) \psi_d(k) + \left(1 - T_s \frac{R_s}{L_q}\right)\psi_q(k) \\ \qquad + T_s u_q(k) + T_s \frac{R_s}{L_q}\psi_{rq}(k) \end{cases} \tag{14}$$

where T_s is the sampling period.

Substituting (11) and (12) into (14), the effective flux linkage at time $k+1$ is represented as:

$$\begin{aligned} &\psi_{ext-f}(k+1) = \\ &\psi_{ext-f}(k) + \left(1 - T_s \frac{R_s}{L_q}\right) L_q i_d(k) + T_s \omega_e(k) \psi_{rq} \\ &+ T_s \omega_e(k) L_q i_q(k) + T_s u_d(k) - L_q i_d^{ref}(k+1) \end{aligned} \tag{15}$$

From the theory of deadbeat control, by setting the effective flux linkage at time $(k+1)$ equal to an appropriate value η, Equation (15) is rewritten as:

$$\eta = \psi_{ext-f}(k) + \left(1 - T_s \frac{R_s}{L_q}\right) L_q i_d(k) + T_s \omega_e(k) \psi_{rq}$$
$$+T_s \omega_e(k) L_q i_q(k) + T_s u_d(k) - L_q i_d^{ref}(k+1) \quad (16)$$

Under the $i_d = 0$ control strategy for the PMSM, Equation (8) indicates that the effective flux linkage under normal operating conditions is:

$$\psi_{ext} = \psi_{r0} \quad (17)$$

According to Equation (7), after permanent magnet demagnetization, an error term $-\psi_{r0} i_d$ appears in T_e. Directly setting $\psi_{ext-f}(k+1)$ equal to ψ_{ext} is therefore unreasonable. Due to the presence of this error term, the post-fault-tolerant Te becomes greater than its normal value, resulting in a larger $i_d^{ref}(k+1)$ than the ideal value. This would cause the stator current to approach its limit. However, the output capability of the inverter is limited, and the stator current cannot exceed its maximum allowable value, which significantly reduces the system's fault tolerance. To achieve better fault tolerance, an appropriate η should be chosen to replace ψ_{ext}, thereby providing a more accurate $i_d^{ref}(k+1)$.

According to the idea of torque deadbeat control, an appropriate η is determined in order to equalize the electromagnetic torque before and after the fault, that is:

$$\frac{3}{2} n_p \left[\eta i_q(k+1) - \psi_{rq} i_d(k+1)\right] = \frac{3}{2} n_p \psi_{ro} i_q(k) \quad (18)$$

From (18), η is obtained as:

$$\eta = \frac{\psi_{ro} i_q(k) + \psi_{rq} i_d(k+1)}{i_q(k+1)} \quad (19)$$

In order to quickly restore the value of i_q after the demagnetization fault to the normal operating value, let

$$i_q(k+1) = i_q(k) \quad (20)$$

Substituting (20) into (19), η is obtained as:

$$\eta = \psi_{ro} + \frac{\psi_{rq} i_d(k+1)}{i_q(k+1)} \quad (21)$$

Substituting the expression for η from Equation (21) in place of $\psi_{ext}(k)$ in Equation (16), $i_d^{ref}(k+1)$ is obtained as:

$$i_d^{ref}(k+1) = \frac{1}{L_q}\left[\psi_{ext-f}(k) - \left[\psi_{ro} + \psi_{rq} \frac{\hat{i}_d(k+1)}{\hat{i}_q(k+1)}\right]\right]$$
$$+\left(1 - \frac{R_s}{L_q} T_s\right) i_d(k)$$
$$+\frac{T_s}{L_q}\left[\omega_e(k) L_q i_q(k) + u_d(k + \omega_e(k) \psi_{rq}\right] \quad (22)$$

where $\hat{i}_d(k+1)$ and $\hat{i}_q(k+1)$ represent the observed values of the predicted d-axis and q-axis currents at the $(k+1)$-th time step, respectively. These observed values can be obtained using the IST-NFTSMO proposed in this paper.

When the PMSM operates normally, $\psi_{rq} = 0$ and $\psi_{ext-f}(k) = \psi_{r0}$. When a demagnetization fault occurs, $\psi_{rq} \neq 0$ and $\psi_{ext-f}(k) \neq \psi_{r0}$. In this case, adjustment is required using the value of $i_d^{ref}(k+1)$ calculated from Equation (22). Furthermore, due to the limited output capability of the inverter, $i_d^{ref}(k+1)$ must satisfy the following constraint:

$$i_d^{ref} > -\sqrt{i_{s\max}^2 - i_q^2} \quad (23)$$

The flowchart of the DFTPC strategy is shown in Figure 2.

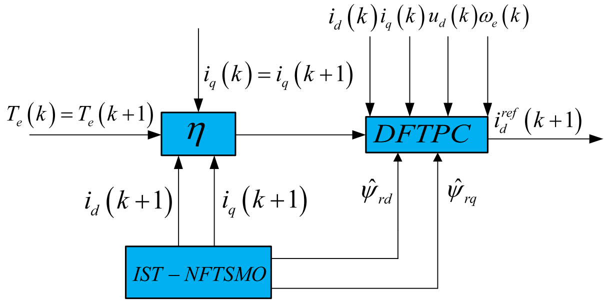

FIGURE 2. The flowchart of DFTPC strategy.

4. DESIGN OF THE IST-NFTSMO FLUX OBSERVER

The key to realizing fault-tolerant predictive control lies in the flux linkage variables. Since flux linkage cannot be directly measured, an observer must be designed. For the system, the following IST-NFTSMO is designed.

Taking the stator current as the state variable, Equation (6) is rewritten in state-space form:

$$\begin{cases} \dot{x} = Ax + Bu + Dd \\ y = Cx \end{cases} \quad (24)$$

where $x = \begin{bmatrix} i_d & i_q \end{bmatrix}^T$, $u = \begin{bmatrix} u_d & u_q \end{bmatrix}^T$, $y = \begin{bmatrix} i_d & i_q \end{bmatrix}^T$, $d = \begin{bmatrix} \psi_{rd} & \psi_{rq} \end{bmatrix}^T$, $A = \begin{bmatrix} -\frac{R_s}{L_d} & \omega_e \frac{L_q}{L_d} \\ -\omega_e \frac{L_d}{L_q} & -\frac{R_s}{L_q} \end{bmatrix}$, $B = \begin{bmatrix} \frac{1}{L_d} & 0 \\ 0 & \frac{1}{L_q} \end{bmatrix}$, $C = \begin{bmatrix} 1 & 0 \\ 0 & 1 \end{bmatrix}$, $D = \begin{bmatrix} 0 & \frac{\omega_e}{L_d} \\ -\frac{\omega_e}{L_q} & 0 \end{bmatrix}$.

To enhance both observer accuracy and suppress chattering in the control input, the observer designed based on Equation (24) is formulated as:

$$\dot{\hat{x}} = Ax + Bu + v \quad (25)$$

where $\hat{x}$is the observed value of x, $\hat{x} = \begin{bmatrix} \hat{i}_d & \hat{i}_q \end{bmatrix}^T$, $v = \begin{bmatrix} v_d & v_q \end{bmatrix}^T$ is the sliding mode term.

Subtracting Equation (25) from Equation (24) yields the current error state equation:

$$\dot{e} = Ae + Dd - v \quad (26)$$

where e is the current observation error,$e = x - \hat{x}$.

To reduce the steady-state error, the non-singular fast terminal sliding mode surface is selected as:

$$s_n = ae + b\dot{e} + \beta \dot{e}^{\frac{p}{q}} \tag{27}$$

where a, b, β are the positive numbers, $a = \operatorname{diag}\left(a_d \;\; a_q\right)$, $b = \operatorname{diag}\left(b_d \;\; b_q\right)$, $\beta = \operatorname{diag}\left(\beta_d \;\; \beta_q\right)$. Both p and q are odd constants to be designed, $1 < p/q<2$.

Taking the derivative of Equation (27) yields:

$$\dot{s}_n = a\dot{e} + b\ddot{e} + \beta \frac{p}{q} \dot{e}^{\frac{p}{q}-1} \ddot{e} \tag{28}$$

To increase the speed at which the system state variables reach the sliding surface, the introduced improved super-twisting control law is:

$$\begin{cases} \dot{s}_n = -k_1 \left|s_n\right|^{\frac{1}{2}} sign(s_n) - k_2 s_n + \sigma \\ \dot{\sigma} = -k_3 sign\left(s_n\right) - k_4 s_n \end{cases} \tag{29}$$

In this article, a linear correction term is introduced into the conventional super-twisting algorithm. As a result, the system is enabled to not only handle disturbances near the origin, but also to suppress the linear growth of disturbances. Meanwhile, the dynamic coupling relationship between s_n and σ is not altered. Therefore, the basic regulation performance of the conventional super-twisting algorithm is maintained.

For the error dynamic equation, the following control law is designed:

$$\begin{cases} v = v_{eq} + v_n \\ v_{eq} = Ae \\ v_n = \int_0^t \left[\frac{a\dot{e}}{b + \beta \frac{p}{q} \dot{e}^{\frac{p}{q}-1}} + k_1 \left|s_n\right|^{\frac{1}{2}} sign\left(s_n\right) - k_2 s_n - \sigma \right] d\tau \\ \dot{\sigma} = -k_3 sign\left(s_n\right) - k_4 s_n \end{cases} \tag{30}$$

where v_n is the switching control law, which improves the state variable to reach the sliding mode surface quickly; v_{eq} is the equivalent control law.

Proof 1: The selected Lyapunov function V_1 is as follows:

$$V_1 = \frac{1}{2} \mathbf{s}_n^2 \tag{31}$$

Taking the derivative of Equation (31) yields:

$$\begin{aligned} \dot{V}_1 &= s_n \dot{s}_n = s_n \left[a\dot{e} + b\ddot{e} + \beta \frac{p}{q} \dot{e}^{\frac{p}{q}-1} \ddot{e} \right] \\ &= s_n \left[a\dot{e} + \left(b + \beta \frac{p}{q} \dot{e}^{\frac{p}{q}-1}\right) \ddot{e} \right] \\ &= s_n \left[\left(b + \beta \frac{p}{q} \dot{e}^{\frac{p}{q}-1}\right) \left(\ddot{e} + \frac{a\dot{e}}{b + \beta \frac{p}{q} \dot{e}^{\frac{p}{q}-1}} \right) \right] \end{aligned} \tag{32}$$

Taking the derivative of Equation (26) yields:

$$\ddot{e} = A\dot{e} + D\dot{d} - \dot{v} \tag{33}$$

Substituting Equation (33) into Equation (32) yields:

$$\dot{V}_1 = s_n \left[\left(b + \beta \frac{p}{q} \dot{e}^{\frac{p}{q}-1}\right) \left(A\dot{e} + D\dot{d} - \dot{v} + \frac{a\dot{e}}{b + \beta \frac{p}{q} \dot{e}^{\frac{p}{q}-1}} \right) \right] \tag{34}$$

Taking the derivative of Equation (26) yields:

$$\begin{cases} \dot{v} = \dot{v}_{eq} + \dot{v}_n \\ \dot{v}_{eq} = A\dot{e} \\ \dot{v}_n = \frac{a\dot{e}}{b + \beta \frac{p}{q} \dot{e}^{\frac{p}{q}-1}} + k_1 \left|s_n\right|^{\frac{1}{2}} sign\left(s_n\right) + k_s s_n - \sigma \\ \dot{\sigma} = -k_3 sign\left(s_n\right) - k_4 s_n \end{cases} \tag{35}$$

Substituting Equation (33) into Equation (32) yields:

$$\begin{aligned} \dot{V}_1 &= s_n \left[\left(b + \beta \frac{p}{q} \dot{e}^{\frac{p}{q}-1}\right) \begin{pmatrix} A\dot{e} + D\dot{d} - A\dot{e} - \frac{a\dot{e}}{b + \beta \frac{p}{q} \dot{e}^{\frac{p}{q}-1}} \\ -k_1 \left|s_n\right|^{\frac{1}{2}} sign\left(s_n\right) - k_2 s_n + \sigma + \frac{a\dot{e}}{b + \beta \frac{p}{q} \dot{e}^{\frac{p}{q}-1}} \end{pmatrix} \right] \\ &= s_n \left[\left(b + \beta \frac{p}{q} \dot{e}^{\frac{p}{q}-1}\right) \left(D\dot{d} - k_1 \left|s_n\right|^{\frac{1}{2}} sign\left(s_n\right) - k_2 s_n + \sigma \right) \right] \\ &= -\left[\left(b + \beta \frac{p}{q} \dot{e}^{\frac{p}{q}-1}\right) \left(-D\dot{d} \cdot s_n + s_n \cdot k_1 \left|s_n\right|^{\frac{1}{2}} + k_2 {s_n}^2 - \sigma s_n \right) \right] \\ &= -\left[\left(b + \beta \frac{p}{q} \dot{e}^{\frac{p}{q}-1}\right) \left(k_2 {s_n}^2 - \sigma s_n + \left|s_n\right| \left(k_1 \left|s_n\right|^{\frac{1}{2}} - D\dot{d} \right) \right) \right] \end{aligned} \tag{36}$$

Equation (36) can also be expressed as:

$$\dot{V}_1 = -\left[\left(b + \beta \frac{p}{q} \dot{e}^{\frac{p}{q}-1}\right) \left(k_1 \left|s_n\right|^{\frac{3}{2}} - \sigma s_n + \left|s_n\right| \left(k_2 \left|s_n\right| - D\dot{d} \right) \right) \right] \tag{37}$$

In actual permanent magnet synchronous motor systems, parameters such as flux linkage, inductance, and resistance may vary, but they are physical quantities whose ranges of variation are limited by the physical structure of the motor and cannot be infinite. Therefore, $\left|D\dot{d}\right|$ is bounded. Since $\left|D\dot{d}\right|$ is bounded, appropriate values of k_1 and k_2 can always be found such that condition $k_1 \left|s_n\right|^{\frac{1}{2}} - \left|D\dot{d}\right| \geq 0$, $k_2 \left|s_n\right| - \left|D\dot{d}\right| \geq 0$ is satisfied, and since $k_2 > 0$, $p/q > 0$, $\dot{e}^{\frac{p}{q}-1} > 0$, while σ and s_n have opposite signs, it can be concluded that:

$$\begin{aligned} \dot{V}_1 &= -\left[\left(b + \beta \frac{p}{q} \dot{e}^{\frac{p}{q}-1}\right) \left(k_2 {s_n}^2 - \sigma s_n + \left|s_n\right| \left(k_1 \left|s_n\right|^{\frac{1}{2}} - D\dot{d} \right) \right) \right] \\ &\leq -\left[\left(b + \beta \frac{p}{q} \dot{e}^{\frac{p}{q}-1}\right) \left(k_2 {s_n}^2 - \sigma s_n + \left|s_n\right| \left(k_1 \left|s_n\right|^{\frac{1}{2}} - \left|D\dot{d}\right| \right) \right) \right] \\ &\leq -\left[\left(b + \beta \frac{p}{q} \dot{e}^{\frac{p}{q}-1}\right) \left(k_2 {s_n}^2 - \sigma s_n \right) \right] \leq 0 \end{aligned} \tag{38}$$

Since $k_1 > 0$ and $k_2 \left|s_n\right| - \left|D\dot{d}\right| \geq 0$, the following is obtained from Equation (37):

$$\begin{aligned} \dot{V}_1 &= -\left[\left(b + \beta \frac{p}{q} \dot{e}^{\frac{p}{q}-1}\right) \left(k_1 \left|s_n\right|^{\frac{3}{2}} - \sigma s_n + \left|s_n\right| \left(k_2 \left|s_n\right| - D\dot{d} \right) \right) \right] \\ &\leq -\left[\left(b + \beta \frac{p}{q} \dot{e}^{\frac{p}{q}-1}\right) \left(k_1 \left|s_n\right|^{\frac{3}{2}} - \sigma s_n + \left|s_n\right| \left(k_2 \left|s_n\right| - \left|D\dot{d}\right| \right) \right) \right] \\ &\leq \left[\left(b + \beta \frac{p}{q} \dot{e}^{\frac{p}{q}-1}\right) \left(k_1 \left|s_n\right|^{\frac{3}{2}} - \sigma s_n \right) \right] \leq 0 \end{aligned} \tag{39}$$

In summary, when $\dot{V}_1 \leq 0$, e will converge to 0 within a finite time, demonstrating that the designed sliding mode observer can achieve a steady state.

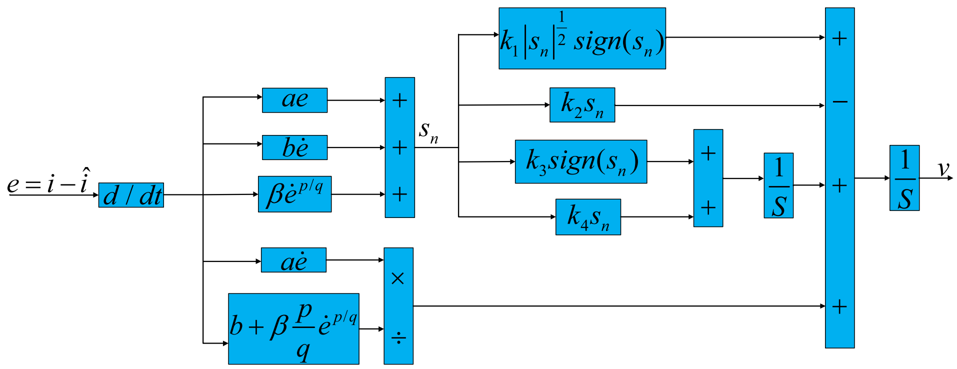

FIGURE 3. The block diagram of IST-NFTSMO.

When the sliding mode observer enters the sliding mode, it is known from the sliding mode equivalence principle that:

$$\dot{e} = e = 0 \tag{40}$$

Substituting Equation (40) into Equation (26) yields:

$$Dd = v \tag{41}$$

Then, the following is obtained from Equation (41):

$$\begin{pmatrix} 0 & \omega_e \\ -\frac{\omega_e}{L_q} & 0 \end{pmatrix} \begin{pmatrix} \hat{\psi}_{rd} \\ \hat{\psi}_{rq} \end{pmatrix} = \begin{pmatrix} v_d \\ v_q \end{pmatrix} \tag{42}$$

From Equation (42), the observed values of the d-q axis flux linkages are obtained as:

$$\begin{cases} \hat{\psi}_{rd} = \frac{-v_q \cdot L_q}{\omega_e} \\ \hat{\psi}_{rq} = \frac{v_d \cdot L_d}{\omega_e} \end{cases} \tag{43}$$

where $\hat{\psi}_{rd}$ and $\hat{\psi}_{rq}$ represent the observed values of the d-q axis flux linkages.

By applying first-order forward Euler discretization to Equation (25), the observed values of the predicted currents at the (k+1)-th time instant are obtained as:

$$\begin{cases} \hat{i}_d(k+1) = \left(1 - \frac{R_s}{L_d}T_s\right)\hat{i}_d(k) \\ +\frac{T_s}{L_d}\left(u_d(k) + \omega_e(k)L_q\hat{i}_q(k) + L_d v_d\right) \\ \hat{i}_q(k+1) = \left(1 - \frac{R_s}{L_q}T_s\right)\hat{i}_q(k) \\ +\frac{T_s}{L_q}\left(u_q(k) - \omega_e(k)L_d\hat{i}_d(k) + L_q v_q\right) \end{cases} \tag{44}$$

The block diagram of the flux linkage observer is shown Figure 3.

5. DESIGN OF THE ISMC

To ensure the stable operation of PMSM under demagnetization faults, an ISMC speed controller incorporating a disturbance observer is designed. Based on an exponential reaching law, the sliding mode controller is formulated, with its state variable expression given as:

$$\begin{cases} e_t = \omega_{ref} - \omega_m \\ \dot{e}_t = \dot{\omega}_{ref} - \dot{\omega}_m = -\dot{\omega}_m \end{cases} \tag{45}$$

where ω_{ref} and ω_m represent the reference speed and actual speed, respectively.

The design of the sliding surface determines the motion quality of the sliding mode. An integral sliding surface can address the issue of high-frequency noise caused by the differentiation of state variables. Therefore, this paper adopts an integral sliding surface function as the sliding surface function, expressed as:

$$s_m = e_t + c_n \int_0^t e_t dt \tag{46}$$

where c_n is an adjustable positive constant.

Taking the derivative of Equation (46) yields:

$$\dot{s}_m = \dot{e}_t + c_n e_t = -\dot{\omega}_m + c_n e_t \tag{47}$$

The mechanical motion equation of a PMSM after a demagnetization fault occurs is:

$$\frac{d\omega_m}{dt} = \frac{3}{2}\frac{n_p}{J}\left[\psi_{r0}i_q + (L_d - L_q)\,i_d i_q + \bigtriangleup\,\psi_{rd}i_q - \psi_{rq}i_d\right]$$
$$-\frac{1}{J}\left(T_L + B\omega_m\right) \tag{48}$$

Equation (48) is rewritten as:

$$\frac{d\omega_m}{dt} = \frac{3}{2}\frac{P_n}{J}\psi_{ro}i_q - \frac{1}{J}\Delta d\left(t\right) - \frac{B}{J}\omega_m \tag{49}$$

where $\Delta d(t)$ represents the total disturbance of the control system.

To address the issue of significant chattering in traditional reaching laws, this paper adopts a novel reaching law:

$$\begin{aligned} &\dot{s}_m = -k_s sign\left(s_m\right) - k_a s_m \\ &k_s = f\left(x_1, s_m\right) + k_t \left|s_m\right|^{\alpha} \\ &f\left(x_1, s_m\right) = \frac{k}{\varepsilon + \left(1 + \frac{1}{|x_1|^n} - \varepsilon\right)e^{-\delta|s|}} \end{aligned} \tag{50}$$

where k_a is the linear gain; k_s is the switching gain; s_m is the sliding surface; x_1 is the system state; $k > 0$, $k_t > 0$, $\delta > 0$, $0 < \varepsilon < 1$; and α is a constant greater than zero.

In the new reaching law, the sign function sign(s_m) can be replaced by the saturation function sat(s_m). The saturation function can, to some extent, suppress the high-frequency chattering caused by the switching of the sliding surface. The saturation function is defined as:

$$sat\left(s_m\right)=\left\{\begin{array}{ll} sign\left(s_m\right) & \left|s_m\right|>\rho \\ \frac{s}{\rho} & \left|s_m\right|<\rho \end{array}\right. \tag{51}$$

In the equation, ρ is the boundary layer value of the function, which determines the smoothness of this saturation function. During the design process, an appropriate value of ρ must be selected.

Combining Equations (47), (49), and (50) yields:

$$\begin{aligned} i_q^* &= \frac{2}{3}\frac{J}{n_p}\frac{1}{\psi_{r0}}\left[\frac{1}{J}d\left(t\right)+\dot{\omega}_{ref}+\frac{B}{J}\omega_m+c_n e_t\right. \\ &\quad \left.+k_s sat\left(s_m\right)+k_a s_m\right] \end{aligned} \tag{52}$$

Proof 2: The selected Lyapunov function V_2 is as follows:

$$V_2=\frac{1}{2}{s_m}^2 \tag{53}$$

Taking the derivative of Equation (31) yields:

$$V_2=s_m\dot{s}_m \tag{54}$$

Combining Equations (47), (49), and (52) yields:

$$\begin{aligned} &V_2=s_m\left[c_n e_t+\dot{\omega}_{ref}-\left(\tfrac{3n_p\psi_{r0}}{2J}i_q^*-\tfrac{1}{J}d\left(t\right)-\tfrac{B}{J}\omega_m\right)\right] \\ &=s_m\left(-k_s sat\left(s_m\right)-k_a s_m\right) \\ &=\left\{\begin{array}{ll} -k_s\left|s_m\right|-k_a s_m^2 & \left|s_m\right|>\rho \\ -\frac{k_s}{\rho}s_m^2-k_a s_m^2 & \left|s_m\right|\leq\rho \end{array}\right. \end{aligned} \tag{55}$$

From Equation (55), the following is obtained:

$$\dot{V}_2=s_m\dot{s}_m\leq 0 \tag{56}$$

According to Lyapunov stability theory, the system employing this sliding mode controller is stable, and any tracking error can converge to zero within a finite time.

The block diagram of the SMDO-based ISMC is shown in Figure 4.

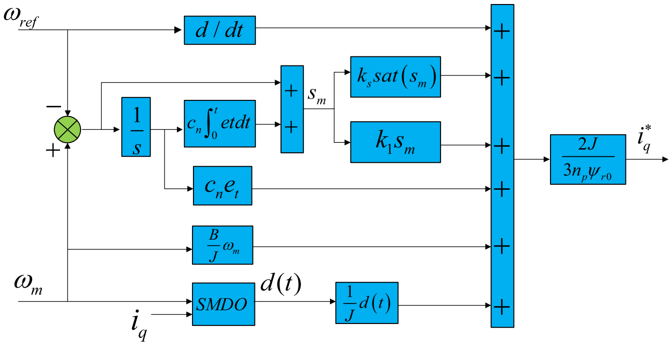

FIGURE 4. The block diagram of ISMC based on SMDO.

The impact of external disturbances $d(t)$ on the control system necessitates the design of a disturbance observer to monitor these external disturbances. The observed value is then fed back to the sliding mode controller to mitigate the influence of external disturbances on its performance.

Considering the presence of external disturbances, the following is derived from Equation (4):

$$\left\{\begin{array}{c} \dot{\omega}_m=-\frac{B}{J}\omega_m-\frac{1}{J}d(t)+\frac{1}{J}T_e \\ \dot{d}(t)=0 \end{array}\right. \tag{57}$$

The state equation of the disturbance observer is:

$$\left\{\begin{array}{c} \dot{\hat{\omega}}_m=-\frac{B}{J}\hat{\omega}_m-\frac{1}{J}\hat{d}(t)+\frac{1}{J}T_e+f(e_m) \\ \dot{\hat{d}}(t)=hf(e_m) \end{array}\right. \tag{58}$$

where $e_m=\omega_m-\hat{\omega}_m$, $f(e_m)$ is the control function of the disturbance observer to be designed.

Subtracting Equation (58) from Equation (57) yields:

$$\left\{\begin{array}{l} \dot{e}_m=-\frac{B}{J}e_m-\frac{1}{J}e_d-f\left(e_m\right) \\ \dot{e}_d=-hf\left(e_m\right) \end{array}\right. \tag{59}$$

In the equation, $e_m=\omega_m-\hat{\omega}_m$ represents the speed observation error, and $e_d=d-\hat{d}$ represents the disturbance observation error.

Select the integral sliding surface:

$$s_d=e_m+c_m\int_0^t e_m dt \tag{60}$$

Taking the derivative of Equation (60) yields:

$$\dot{s}_d=\dot{e}_m+c_m e_m \tag{61}$$

Select the reaching law:

$$\dot{s}_d=-k_m sign\left(s_m\right) \tag{62}$$

where k_m is the switching gain of the reaching law.

By treating $-\frac{e_d}{J}$ as a disturbance term, the control law for the sliding mode disturbance observer is formulated as:

$$f\left(e_m\right)=k_m sign\left(s_d\right)+\left(c_m-\frac{B}{J}\right)e_m \tag{63}$$

Under the action of the control law, the system trajectory can reach and remain on the sliding mode surface within a finite time. It can be concluded that:

$$s_d=\dot{s}_d=0 \tag{64}$$

$$e_m=\dot{e}_m \tag{65}$$

From Equation (59), it can be obtained that:

$$\left\{\begin{array}{l} e_d=-Jf\left(e_m\right) \\ \dot{e}_d=-hf\left(e_m\right) \end{array}\right. \tag{66}$$

From Equation (66), it can be obtained that:

$$e_d=c_T e^{\frac{l}{J}t} \tag{67}$$

where c_T is a constant.

Proof 3: The selected Lyapunov function V_3 is as follows:

$$V_3=\frac{1}{2}s_d^2 \tag{68}$$

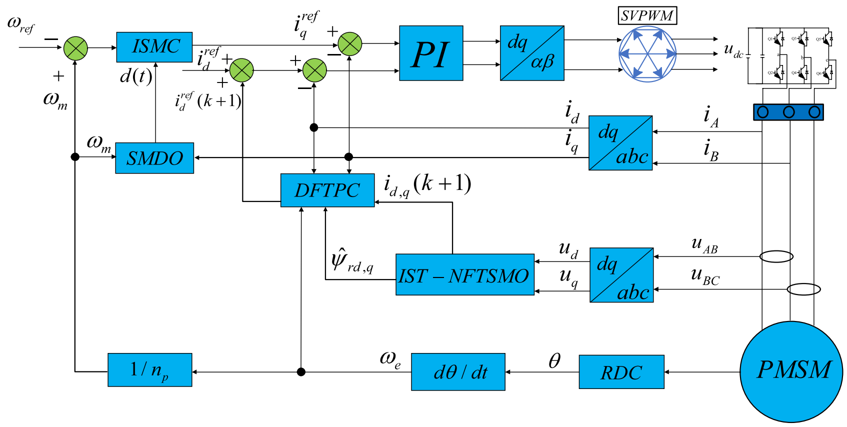

FIGURE 5. The system block diagram of IST-NFTSMO-based DFTPC.

Taking the derivative of Equation (68) yields:

$$\dot{V}_3 = s_d\dot{s}_d \tag{69}$$

Combining Equations (59), (61), and (63) yields:

$$\begin{aligned}\dot{V}_3 &= s_d\dot{s}_d = s_d\left(c_m e_m - \frac{B}{J}e_m - \frac{1}{J}e_d - g\left(e_m\right)\right)\\ &= s_d\left(-k_m sign\left(s_d\right) - \frac{e_d}{J}\right)\end{aligned} \tag{70}$$

According to Lyapunov stability theory, it can be obtained that:

$$\dot{V}_3 = s_d\dot{s}_d < 0 \tag{71}$$

From Equation (71), it can be obtained that:

$$k_m > \frac{|e_d|}{J} \tag{72}$$

Equation (72) indicates that when the load disturbance observation error is large, the observer switching gain needs to increase accordingly, which leads to enhanced chattering in the observed values.

To address the above issue, the switching gain of the observer is designed as a function of the disturbance observation error e_T:

$$k_m = f_\varepsilon\frac{|e_d|}{J} \tag{73}$$

where f_ε is a constant greater than 1. When the load observation error is large, the switching gain increases accordingly to ensure system stability. Conversely, when the load disturbance observation error is small, the switching gain remains low, which helps mitigate sliding-mode chattering in the observed values.

The system block diagram of IST-NFTSMO-based DFTPC is shown in Figure 5.

6. EXPERIMENTAL RESULTS AND ANALYSIS

Since demagnetization faults in PMSM are challenging to replicate in physical motors, a hardware-in-the-loop (HIL) simulation platform was established using RT-LAB to verify the effectiveness and feasibility of the proposed fault-tolerant predictive control strategy for demagnetization faults, without compromising the validity of the experimental results. As illustrated in Figure 6, a TMS320F2812 DSP was utilized, while other system components, including the PMSM and the inverter, were constructed using the RT-LAB (OP5600) system from Opal-RT.

For the PMSM, the $i_d = 0$ control strategy was employed. Table 1 presents the nominal parameters of the motor, and Table 2 lists the control parameters of the control methods as well as the parameters of the observer.

TABLE 1. Parameters of PMSM.

Parameter		Value
DC voltage	u_{dc}	1500 V
Number of pole pairs	n_p	4
Stator resistance	R_s	0.02 Ω
d-axis inductance	L_d	0.0015 H
q-axis inductance	L_q	0.003572 H
PM flux linkage	ψ_{ro}	0.892 Wb
Rotational inertia	J	1 kg·m^2
Viscous friction coefficient	B	0.001 N·m·s/rad

TABLE 2. Parameters of the control system and parameters of the observer.

PI	ISMC	SMO	IST-NFTSMO
$k_p = 150$	$c_n = 0.01$	$k_d = 50000$	$a = 20$
$k_i = 5000$	$k = 107.5$	$k_q = 50000$	$b = 4$
	$\varepsilon = 0.1$		$\beta = 0.01$
	$n = 0.08$		$p/q = 5/7$
	$\delta = 9.9$		$k_1 = 50$
	$k_t = 0.01$		$k_2 = 6500$
	$\alpha = 0.1$		$k_3 = 20$
	$k_a = 0.05$		$k_4 = 10$
	$\rho = 0.1$		

First, proportional-integral (PI) control without the DFTPC algorithm and ISMC without the DFTPC algorithm were compared. Next, PI control with the DFTPC algorithm and ISMC with the DFTPC algorithm were compared. Finally, the flux linkages observed by the SMO and the IST-NFTSMO were experimentally compared.

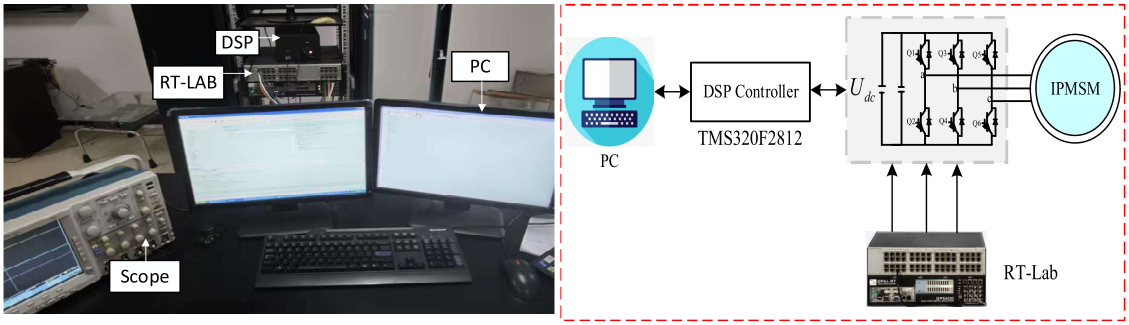

FIGURE 6. RT-LAB experiment platform and RT-LAB hardware-in-the-loop system configuration.

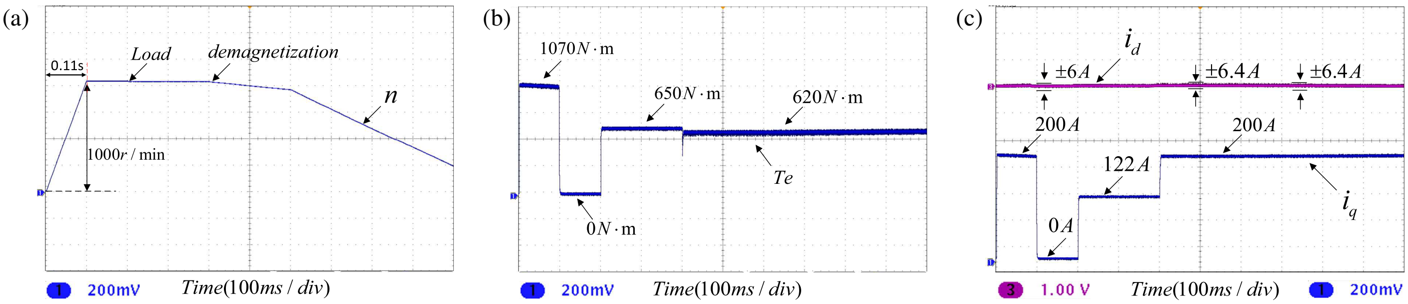

FIGURE 7. Experimental results of PI control without DFTPC algorithm.

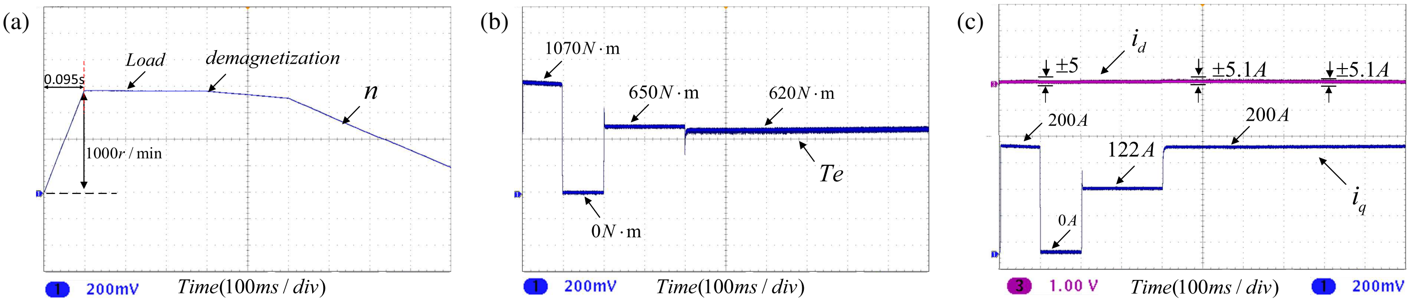

FIGURE 8. Experimental results of ISMC control without DFTPC algorithm.

The motor was started under no-load conditions with a reference speed set to 1000 r/min. At 0.2 s, the load torque T_L was increased from 0 N·m to 650 N·m. At 0.4 s, a demagnetization fault occurred in the PMSM, where the permanent magnet flux amplitude decreased from 0.892 Wb to 0.6 Wb, and the magnetic deflection angle changed from 0 rad to $\pi/6$ rad. At 0.6 s, the load torque was further increased from 650 N·m to 800 N·m. The total experiment duration was 1 s.

Figures 7 and 8 present the experimental results for PI control and ISMC, respectively, without the DFTPC algorithm under demagnetization fault conditions. Among them, Figures 7(a) and 8(a) show the response curves of the d-q axis currents; Figures 7(b) and 8(b) display the output torque curves; and Figures 7(c) and 8(c) illustrate the speed curves. Table 3 comparison of comprehensive control performance without the DFTPC algorithm.

From Figures 7(a) and 8(a), it can be observed that after no-load starting of the motor, the ISMC reaches the reference speed at 0.095s, whereas the PI controller reaches it at 0.11 s. During no-load starting, the PI controller exhibits a speed overshoot of 0.1%, while the novel sliding mode speed controller proposed in this paper shows almost no overshoot. At 0.2 s, when the load is applied, the speed under PI control decreases by 5 r/min, whereas under ISMC it decreases by only 2.2 r/min. At 0.4 s, when permanent magnet demagnetization occurs, the i_q of both PI and ISMC rapidly increases to the limit value of 200 A. At this point, i_q is insufficient to maintain Te stability; therefore, the Te output by both control methods is less than T_L, leading to a speed drop. At 0.6 s, when T_L is further increased to 800 N·m, the speed under both control methods drops more rapidly and fails to track the rated speed.

TABLE 3. Comparison of control methods without the DFTPC algorithm.

variable	PI	ISMC
i_d	0/0/0/0/0	0/0/0/0/0
i_q	200/0/122/200/200	200/0/122/200/200
T_e	1070/0/650/620/620	1070/0/650/620/620

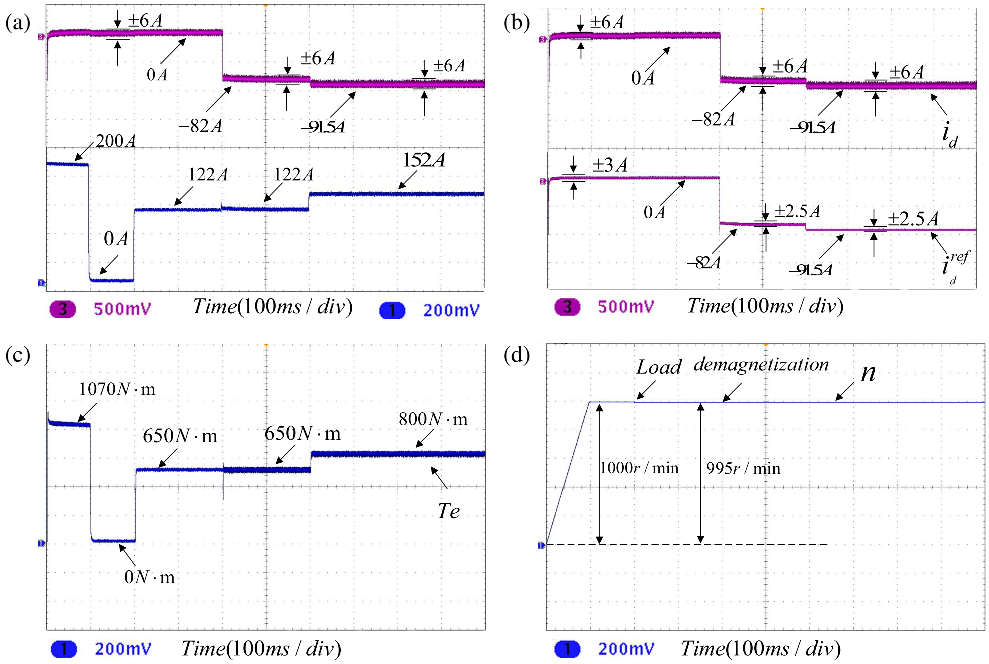

FIGURE 9. PI control with the DFTPC algorithm.

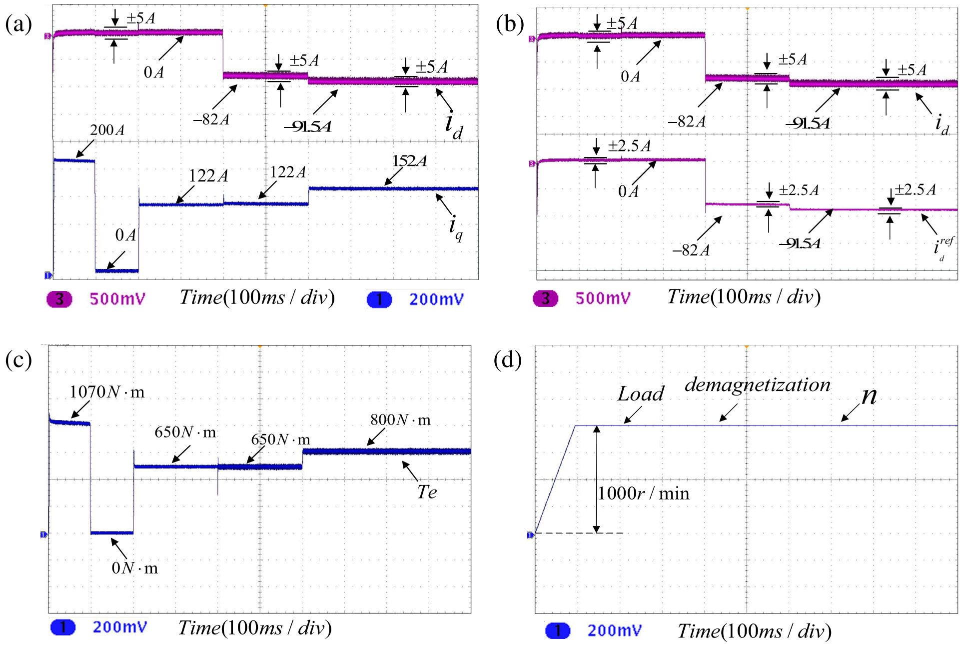

FIGURE 10. ISMC control with the DFTPC algorithm.

In summary, when the motor operates under normal conditions, the ISMC demonstrates faster dynamic response and stronger stability than the traditional PI control. However, due to the lack of regulation from the DFTPC algorithm, when a demagnetization fault occurs in the PMSM, the novel sliding mode speed controller proposed in this paper still cannot maintain normal motor operation at the rated speed.

Figures 9 and 10 present the experimental results for PI control and ISMC, respectively, both employing the DFTPC algorithm. Specifically, Figures 9(a) and 10(a) show the response curves of the d-q axis currents. Figures 9(b) and 10(b) display the comparative curves between the d-axis current and its reference value. Figures 9(c) and 10(c) illustrate the electromagnetic torque curves. Finally, Figures 9(d) and 10(d) depict the speed curves. Table 4 comparison of comprehensive control performance with the DFTPC algorithm.

From Figures 9(a) and 10(a), it can be observed that after no-load startup of the motor, the reference speed is reached at 0.095 s under ISMC, while under PI control, it is reached at 0.11 s. The speed overshoot during no-load startup is 0.1%

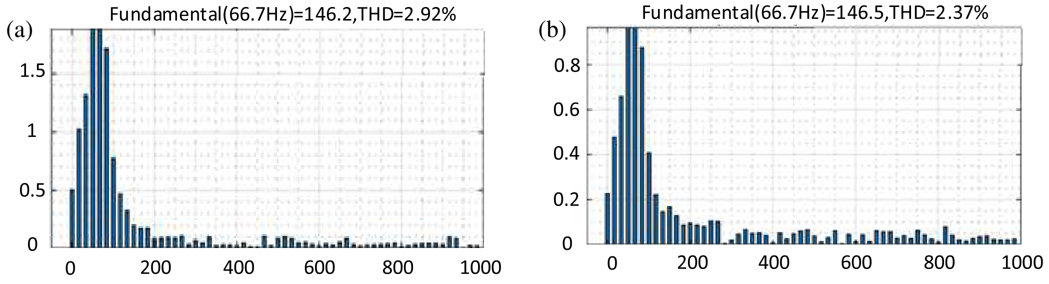

FIGURE 11. THD analysis of phase A stator current.

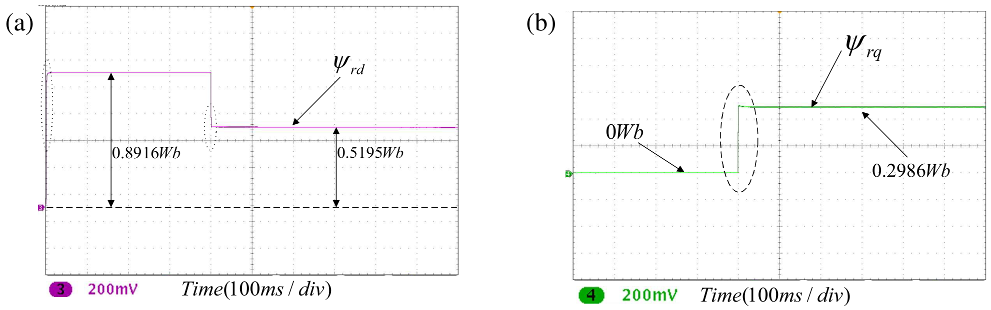

FIGURE 12. Observed values of the SMO.

TABLE 4. Comparison of control methods with the DFTPC algorithm.

variable	PI	ISMC
i_d	0/0/0/-82/-91.5	0/0/0/-82/-91.5
i_q	200/0/122/122/152	200/0/122/122/152
T_e	1070/0/650/650/800	1070/0/650/650/800

for PI control, whereas the proposed novel sliding mode speed controller exhibits almost no overshoot. Under no-load motor startup, a load torque of 650 N·m is applied at 0.2 s, during which the reference current for the d-axis at the next time instant, as output by the DFTPC algorithm, remains at 0. At 0.4 s, demagnetization of the permanent magnet occurs while the load torque is still maintained at 650 N·m. At this moment, the reference current for the d-axis at the next time instant, output by the DFTPC algorithm, decreases from 0 to -82 A. The calculated constraint value for i_d is -158.5 A, indicating that $i_d^{ref}(k+1)$ remains within the constraint range.

At 0.4 s, permanent magnet demagnetization occurs. The ψ_d observed by the proposed IST-NFTSMO decreases from 0.892 Wb to 0.52 Wb, while the observed ψ_q increases from 0 Wb to 0.3 Wb. These values align with the theoretically calculated values of 0.5196 Wb and 0.3 Wb, respectively. Therefore, the proposed IST-NFTSMO is capable of accurately observing the flux linkages.

At 0.6 s, the load torque changes from 650 N·m to 800 N·m. The value of i_d^{ref} decreases from -82.5 A to -91.5 A. Under the load torque of 800 N·m, the calculated constraint value for i_d is -130.0 A, indicating that $i_d^{ref}(k+1)$ remains within the constraint range.

Figures 11(a) and 11(b) show the THD results of the phase A stator current for DFTPC-PI and DFTPC-ISMC, respectively. During the permanent magnet demagnetization period from 0.4s to 0.6 s, the waveforms are analyzed. The THD values for the DFTPC-PI and DFTPC-ISMC methods are 2.92% and 2.37%, respectively. The results indicate that compared to DFTPC-PI, the DFTPC-ISMC method proposed in this paper can effectively suppress the current harmonics after a demagnetization fault occurs in the PMSM.

In summary, compared with conventional PI control, the DFTPC algorithm demonstrates stronger stability in the control system. After no-load startup of the motor, the speed convergence time is improved by 13.6%, and the total harmonic distortion (THD) of the phase A stator current is reduced by 18.8%. Following the occurrence of a demagnetization fault at 0.4 s, the torque recovery shows an improvement of 4.8%; after the load torque is applied at 0.6 s, the torque recovery improvement reaches 29%. Moreover, the system is capable of driving larger loads after a demagnetization fault occurs in the PMSM. In comparison with DFTPC-PI, the DFTPC-ISMC proposed in this paper exhibits stronger stability, smaller speed fluctuations, lower harmonic content, and superior anti-interference performance.

Figures 12 and 13 present the comparative experimental results for the conventional SMO and the IST-NFTSMO, respectively. Specifically, Figure 12(a) and Figure 13(a) show the observed results for the d-axis flux linkage, while Figure 12(b) and Figure 13(b) display the experimental results for the q-axis flux linkage.

Before 0.4 s, the motor starts under no-load and operates normally. The d-axis flux linkage observed by the SMO reaches its steady-state value of 0.8916 Wb at 0.11 s, whereas the IST-NFTSMO reaches its steady-state value of 0.892 Wb at 0.09 s. The q-axis flux linkage observed by both observers is maintained at 0 Wb. At 0.4 s, when the permanent magnet demag-

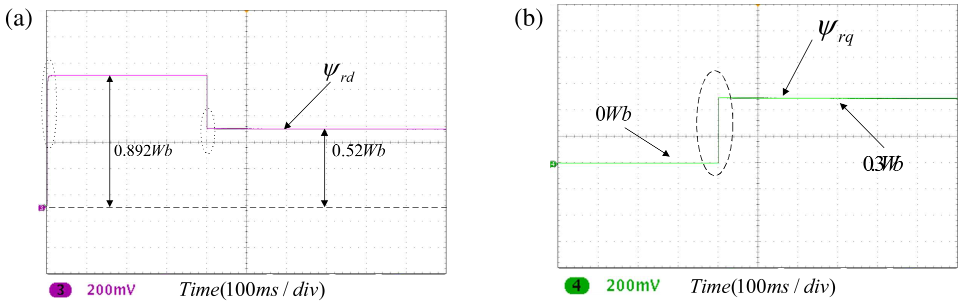

FIGURE 13. Observed values of the IST-NFTSMO.

netizes, the d-axis flux linkage observed by the SMO reaches its steady-state value of 0.5195 Wb at 0.48 s, and the observed q-axis flux linkage reaches its steady-state value of 0.2986 Wb at 0.52 s. In comparison, the d-axis flux linkage observed by the IST-NFTSMO reaches its steady-state value of 0.52 Wb at 0.45 s, and the observed q-axis flux linkage reaches its steady-state value of 0.3 Wb at 0.48 s.

In summary, compared with the conventional SMO, the IST-NFTSMO demonstrates faster observation speed, more accurate observed values, and smoother flux linkage waveforms. Therefore, the IST-NFTSMO exhibits superior dynamic performance, stronger stability, and less chattering.

7. CONCLUSION

To address the issue of degraded control performance and the difficulty in achieving high-performance control in PMSMs following a demagnetization fault, a deadbeat fault-tolerant control strategy based on an improved sliding mode observer is proposed for permanent magnet synchronous motors with demagnetization faults. This method achieves precise observation of the permanent magnet flux linkage while accurately compensating for torque. Through experimental analysis under various operating conditions, the following conclusions are drawn:

(1) The designed IST-NFTSMO enables online monitoring of the permanent magnet flux linkage. Under normal PMSM operation, it accurately observes the flux linkage components on the d-axis and q-axis, respectively. When a demagnetization fault occurs, it rapidly converges from the normal value to the fault value. The observed flux linkage is fed back to the controller, thereby eliminating the influence of flux linkage parameter mismatch.

(2) When combined with conventional PI control and the ISMC, the DFTPC algorithm promptly outputs $i_d^{ref}(k+1)$, compensates for the torque deficit, and suppresses sudden surges in i_q. This ensures stable motor operation under demagnetization fault conditions, exhibiting stronger stability and fault tolerance.

(3) After combining the proposed ISMC with the SMDO, the anti-interference capability of the system is significantly improved. Compared with PI control, the speed convergence time is reduced by 13.6%, and the total harmonic distortion (THD) of the phase A stator current is reduced by 18.8%.

ACKNOWLEDGEMENT

This work was supported by the Scientific Research Fund of Hunan Provincial Education Department under Grant Number 24A0395.

REFERENCES

[1] Wang, F., Y. Wei, H. Young, D. Ke, H. Xie, and J. Rodríguez, "Continuous-control-set model-free predictive fundamental current control for PMSM system," *IEEE Transactions on Power Electronics*, Vol. 38, No. 5, 5928–5938, May 2023.

[2] Wei, Y., H. Young, D. Ke, D. Huang, F. Wang, and J. Rodríguez, "Adaptive ultralocalized time-series for improved model-free predictive current control on PMSM drives," *IEEE Transactions on Power Electronics*, Vol. 39, No. 5, 5155–5165, May 2024.

[3] Zhu, L., B. Xu, and H. Zhu, "Interior permanent magnet synchronous motor dead-time compensation combined with extended kalman and neural network bandpass filter," *Progress In Electromagnetics Research M*, Vol. 98, 193–203, 2020.

[4] Zhang, Y., J. Jin, and L. Huang, "Model-free predictive current control of PMSM drives based on extended state observer using ultralocal model," *IEEE Transactions on Industrial Electronics*, Vol. 68, No. 2, 993–1003, Feb. 2021.

[5] Sarlioglu, B., C. T. Morris, D. Han, and S. Li, "Driving toward accessibility: A review of technological improvements for electric machines, power electronics, and batteries for electric and hybrid vehicles," *IEEE Industry Applications Magazine*, Vol. 23, No. 1, 14–25, Jan.–Feb. 2017.

[6] Dong, H., H. Ma, Z. Wang, J. Man, L. Jia, and Y. Qin, "An online health monitoring framework for traction motors in high-speed trains using temperature signals," *IEEE Transactions on Industrial Informatics*, Vol. 19, No. 2, 1389–1400, Feb. 2023.

[7] Cheng, M., J. Hang, and J. Zhang, "Overview of fault diagnosis theory and method for permanent magnet machine," *Chinese Journal of Electrical Engineering*, Vol. 1, No. 1, 21–36, 2015.

[8] Bhuiyan, E. A., M. M. A. Akhand, S. K. Das, M. F. Ali, Z. Tasneem, M. R. Islam, D. K. Saha, F. R. Badal, M. H. Ahamed, and S. I. Moyeen, "A survey on fault diagnosis and fault tolerant methodologies for permanent magnet synchronous machines," *International Journal of Automation and Computing*, Vol. 17, No. 6, 763–787, 2020.

[9] Candelo-Zuluaga, C., J.-R. Riba, D. V. Thangamuthu, and A. Garcia, "Detection of partial demagnetization faults in five-phase permanent magnet assisted synchronous reluctance machines," *Energies*, Vol. 13, No. 13, 3496, Jul. 2020.

[10] Krichen, M., E. Elbouchikhi, N. Benhadj, M. Chaieb, M. Benbouzid, and R. Neji, "Motor current signature analysis-based permanent magnet synchronous motor demagnetization characteri-

zation and detection," *Machines*, Vol. 8, No. 3, 35, 2020.

[11] Zhu, M., W. Hu, and N. C. Kar, "Acoustic noise-based uniform permanent-magnet demagnetization detection in SPMSM for high-performance PMSM drive," *IEEE Transactions on Transportation Electrification*, Vol. 4, No. 1, 303–313, Mar. 2018.

[12] Ishikawa, T. and N. Igarashi, "Failure diagnosis of demagnetization in interior permanent magnet synchronous motors using vibration characteristics," *Applied Sciences*, Vol. 9, No. 15, 3111, Aug. 2019.

[13] Xu, Z., J. Zhang, Y. Jiang, *et al.*, "Detection of local demagnetization in permanent magnet synchronous machine based on high frequency signal injection," *Proceedings of the CSEE*, Vol. 45, No. 8, 3205–3214, Apr. 2025.

[14] Eker, M. and B. Gündogan, "Demagnetization fault detection of permanent magnet synchronous motor with convolutional neural network," *Electrical Engineering*, Vol. 105, No. 3, 1695–1708, 2023.

[15] Song, J., S. Liu, Z. Duan, X. Wu, W. Ding, X. Wang, and S. Lu, "Dpmslm demagnetization fault detection based on texture feature analysis of grayscale fusion image," *IEEE Transactions on Instrumentation and Measurement*, Vol. 72, 1–12, 2023.

[16] Zhang, C., M. Zhang, J. He, R. Shao, and L. Luo, "Demagnetization faults robust detection method based on an adaptive sliding mode observer for PMSM," *Journal of Advanced Computational Intelligence and Intelligent Informatics*, Vol. 20, No. 7, 1127–1134, 2016.

[17] Zhang, C., M. Y. Zhang, F. M. Zhang, *et al.*, "A cascade observer to detect demagnetization faults for PMSM," *Electric Machines and Control*, Vol. 21, No. 2, 45–54, 2017.

[18] Gao, J., W. Gui, C. Yang, T. Peng, J. Luo, and Y. Han, "Multiple observers-based demagnetization fault detection with inductance mismatch impacts eliminated for PMSMs," *IEEE Transactions on Power Electronics*, Vol. 38, No. 7, 8016–8021, Jul. 2023.

[19] Zhao, J., L. Wang, L. Xu, F. Dong, J. Song, and X. Yang, "Uniform demagnetization diagnosis for permanent-magnet synchronous linear motor using a sliding-mode velocity controller and an ALN-MRAS flux observer," *IEEE Transactions on Industrial Electronics*, Vol. 69, No. 1, 890–899, Jan. 2022.

[20] Zhao, K., R. Zhou, J. She, C. Zhang, J. He, G. Huang, and X. Li, "Demagnetization-fault reconstruction and tolerant-control for PMSM using improved SMO-based equivalent-input-disturbance approach," *IEEE/ASME Transactions on Mechatronics*, Vol. 27, No. 2, 701–712, Apr. 2022.

[21] Zhang, C., G. Wu, J. He, and K. Zhao, "Sliding observer-based demagnetization fault-tolerant control in permanent magnet synchronous motors," *The Journal of Engineering*, 175–183, 2017.

[22] Wang, T., A. Y. Wang, Y. X. Jin, and J. Sun, "Research on fault-tolerant control method for demagnetization faults of permanent magnet synchronous motor," in *2018 IEEE Student Conference on Electric Machines and Systems*, 1–6, Huzhou, China, Dec. 2018.

[23] Wang, Q., G. Wang, N. Zhao, G. Zhang, Q. Cui, and D. Xu, "An impedance model-based multiparameter identification method of PMSM for both offline and online conditions," *IEEE Transactions on Power Electronics*, Vol. 36, No. 1, 727–738, Jan. 2021.

[24] Verkroost, L., J. D. Bisschop, H. Vansompel, F. D. Belie, and P. Sergeant, "Active demagnetization fault compensation for axial flux permanent-magnet synchronous machines using an analytical inverse model," *IEEE Transactions on Energy Conversion*, Vol. 35, No. 2, 591–599, Jun. 2020.

[25] Zhang, C., G. Wu, F. Rong, J. Feng, L. Jia, J. He, and S. Huang, "Robust fault-tolerant predictive current control for permanent magnet synchronous motors considering demagnetization fault," *IEEE Transactions on Industrial Electronics*, Vol. 65, No. 7, 5324–5334, 2018.

[26] Lei, J., S. Fang, D. Huang, and Y. Wang, "Enhanced deadbeat predictive current control for PMSM drives using iterative sliding mode observer," *IEEE Transactions on Power Electronics*, Vol. 38, No. 11, 13 866–13 876, Nov. 2023.

[27] Zhao, K., A. Leng, R. Zhou, W. Dai, S. Wu, and T. Li, "Demagnetization fault reconstruction for six-phase permanent magnet synchronous motor by improved super-twisting algorithm-based sliding-mode observer," *Measurement*, Vol. 172, 108905, Feb. 2021.